

VISUALIZING NUCLEOSOME PHASE SEPARATION WITH SUPER RESOLUTION  
MICROSCOPY

PHD PRELIMINARY EXAMINATION

DEPARTMENT OF PHYSICS

BY  
CLAYTON W. SEITZ

FALL 2023

# TABLE OF CONTENTS

ABSTRACT . . . . .	iii
0.1 Introduction . . . . .	1
0.1.1 Single molecule localization microscopy . . . . .	1
0.1.2 Novel approaches to time-resolved SMLM . . . . .	2
0.1.3 Visualizing nucleosome-BRD4 interactions at super-resolution . . . . .	4
0.2 Results . . . . .	6
0.2.1 Novel approaches to time-resolved SMLM . . . . .	6
0.2.2 Visualizing nucleosome clusters at super-resolution . . . . .	8
0.3 Future Aims . . . . .	10
0.3.1 Specific Aim 1: Measure nucleosome cluster dynamics in living cells . . . . .	10
0.3.2 Specific Aim 2: Determine effects of JQ1 and 1,6 Hexanediol exposure on nucleosome organization . . . . .	11
0.4 Materials and Methods . . . . .	12
0.4.1 Super-resolution imaging of nucleosome nanodomains . . . . .	12
0.4.2 Localization with maximum likelihood estimation . . . . .	13
0.4.3 Dense localization with convolutional neural networks . . . . .	15
0.4.4 Dense localization by fluorescence antibunching . . . . .	16
0.4.5 Computation of Ripley’s L-function . . . . .	16
0.4.6 Fourier Ring Correlation . . . . .	16
0.5 Supplemental Information . . . . .	18
0.5.1 Estimator precision sets the resolution limit in localization microscopy . . . . .	18
0.5.2 Integrated isotropic and anisotropic Gaussian point spread functions . . . . .	19
0.6 References . . . . .	20

# ABSTRACT

Single-molecule localization microscopy (SMLM) techniques, such as direct stochastic optical reconstruction microscopy (dSTORM), can be used to produce a pointillist representation of nucleosome organization at diffraction-unlimited precision. Direct STORM approaches leverage the deactivation of standard fluorescent tags, followed by spontaneous or photoinduced reactivation, which can be used to achieve super-resolution reconstructions of nuclear proteins and nucleic acids. This basic principle remains one of the method's primary limitations - standard SMLM fitting routines require tight control of activation and reactivation to maintain sparse emitters, presenting a tradeoff between imaging speed and labeling density. Here, I present problem-oriented strategies for dense stochastic optical reconstruction of nucleosome organization in living cell nuclei. The first complements high duty-cycle blinking of nucleosome-bound dyes with a localization algorithm based on a deep neural networks. The second utilizes sub-Poisson photon statistics to deconvolve nearby emitters with a photon counting camera. The former technique is then demonstrated by live cell imaging of chromatin nanodomains and physical analysis of their associations with BRD4 - a well known component of phase separated condensates in the nucleus.

## 0.1 Introduction

### 0.1.1 *Single molecule localization microscopy*

Single molecule localization microscopy (SMLM) relies on the temporal resolution of fluorophores in the sample whose spatially overlapping point spread functions would otherwise render them unresolvable at the detector. SMLM techniques, such as stochastic optical reconstruction microscopy (STORM) and photo-activated localization microscopy (PALM) remain desirable for super-resolution imaging of many cellular structures, due to their cost-effective implementation and diffraction unlimited resolution (Schermerle 2019). Common strategies for the temporal separation of molecules involve transient intramolecular rearrangements to switch from dark to fluorescent states or the exploitation of non-emitting molecular radicals. For direct STORM, rhodamine derivatives can undergo intersystem crossing to a triplet state, which can be reduced by thiols to form a dark radical species. The dark state can then be quenched by oxidative processes, driving the fluorophore back to its ground state (Figure 1). Long dark state lifetimes are commonly used in STORM imaging, while quenching results in higher duty cycle photoswitching and increased rates of photobleaching due to irreversible oxidative damage of important functional groups.

The spatial resolution of SMLM images is limited only by the variance of a statistical estimator of molecular coordinates. This variance is an aleatoric or systematic uncertainty, typically of a maximum likelihood estimator, and is bounded from below by the Cramer-Rao lower bound (Chao 2016). Localization uncertainties are commonly tens of nanometers, although recent work on integration of Bayesian priors with modulation enhanced single molecule localization microscopy (meSMLM) has reduced spatial resolution below 1 nanometer (Kalisvaart 2022). However, fluorescent labeling density still remains a major bottleneck to SMLM acquisitions. Static uncertainty due to molecular crowding can be partially ameliorated by using pairwise or higher-order temporal correlations within a pixel neighborhood,

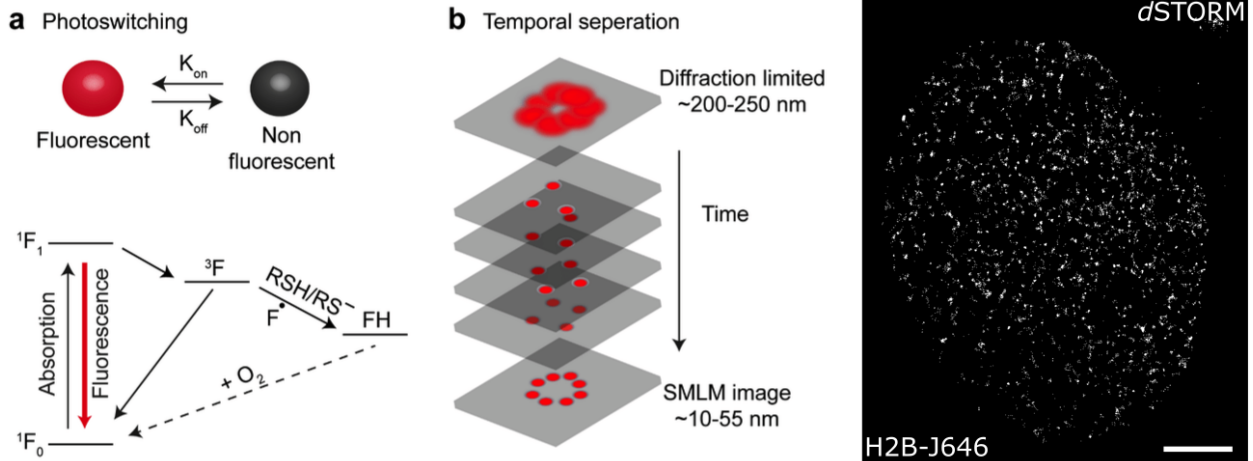


**Figure 1: Stochastic optical reconstruction microscopy (STORM).** (A) Single molecules are resolved by separating their fluorescent emission in time, using fluorophores with multiple photophysical states (B) Example super-resolution image of H2B protein in a living HeLa cell nucleus and the first frame of a STORM time series (inset). (C) Photophysics of tetramethylrhodamine (TMR) and its derivatives JF549 and JF646. Maximum absorption occurs at 549nm or 646nm respectively and return to the ground state can occur via twisted internal charge transfer or inter-system crossing (Grimm 2021)

known as stochastic optical fluctuation imaging (Dertinger 2009). Other approaches such as stimulated emission and depletion (STED) imaging bring control over the photophysical state of a chosen subset of the sample, yet the need for laser scanning prevents widespread application in live-cell studies. Furthermore, the spatial resolution and relative simplicity of SMLM techniques remains unmatched, inciting an effort to increase the time resolution of STORM and PALM methods.

Mention that this is classical photon statistics

### 0.1.2 Novel approaches to time-resolved SMLM

Previous approaches to improving time resolution in SMLM have been primarily based on probabilistic deep learning. In particular, deep generative models learn prior information about cellular structures from super-resolution images, which is used to predict super-resolution images based on sparse localizations or widefield images (Ouyang 2018; Barth

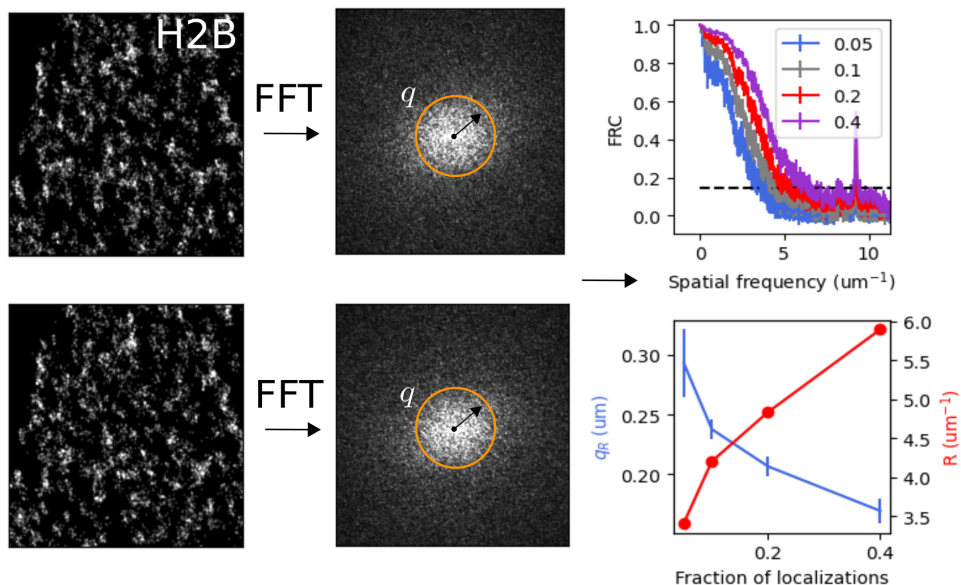


**Figure 2: Dense localization increases image resolution and enables time-resolved STORM.** A pair of subsets is drawn from the full list of localizations, and isotropic Gaussian kernel density estimation is performed. The Fourier Ring Correlation is calculated for the pair and plotted as a function of spatial frequency.

2020; Chen 2023). Other approaches use convolutional neural networks to interpolate and transform dense images into a localization map (Nehme 2020; Speiser 2021). All of these approaches either directly or indirectly address the problem of molecular counting and localization in dense fluorescence images. Here, we will explore a particular deep learning technique called DeepSTORM3D as well as more our own methods, which replace sCMOS cameras with single photon counting cameras.

Within the broader domain of super-resolution imaging, innovations in single photon detection technologies have begun to be integrated into fluorescence microscopes (Forbes 2019). Single photon detectors such as single photon avalanche photodiodes (SPADs) have orders of magnitude higher temporal resolutions than standard sCMOS cameras, single photon sensitivity, and theoretically zero readout noise. Such properties make these devices highly desirable for imaging applications; however, application of SPAD arrays in imaging have been limited to small bundles of a few tens of detector elements combined with laser

scanning (Israel 2017; Forbes 2019; Tenne 2019). Recently, SPAD cameras have become commercially available, potentially bringing many of the advantages of single photon detection to widefield fluorescence microscopy.

Isolated fluorescent emitters exhibit fluorescence antibunching, which means that fluorescence emission has sub-Poisson photon statistics. This property of fluorescence emission from a single emitter has been previously applied to counting fluorescent molecules in the spot of a confocal microscope (Ta 2010). Molecular counting with photon statistics has a fairly simple motivation: a photon emitted by a fluorescence molecule can only be detected once. Coincidence of photons at multiple detector elements provides evidence that two or more molecules are present in the imaged region. Therefore, we propose an online parameter estimation technique which utilizes fluorescence antibunching to localize molecules in widefield images collected on a 512 pixel x 512 pixel SPAD camera.

### *0.1.3 Visualizing nucleosome-BRD4 interactions at super-resolution*

The nucleosome is the fundamental unit of chromatin, which forms the basic scaffold for a variety of biomolecular processes in a cell nucleus. Super-resolved nucleosome organization has been studied extensively in various epigenomic states to reveal segregated nanoclusters, dispersed nanodomains, and compact large aggregates. Nucleosomes assemble into heterogeneous clusters of variable sizes, interspersed with nucleosome-depleted regions (Ricci 2015). Histones can be decorated with various post-translational modifications such as acetylation, methylation, phosphorylation, and ubiquitination. The recruitment of proteins and complexes with specific enzymatic activities is now a well-accepted dogma of how modifications mediate their function. Histone modifications can influence transcription of genes, and many other DNA processes such as repair, replication and recombination (Bannister and Kouzarides, 2011).

Here, we apply super-resolution techniques to study live-cell dynamics of nucleosome or-

ganization, with a particular focus on the structure of biomolecular condensates containing bromodomain protein 4 (BRD4) protein, a major tandem-bromodomain-containing transcriptional regulator. BRD4 plays an important role in diverse cellular functions such as transcription, replication, epigenetic regulation, and DNA repair, and has been implicated in cancer and autoimmune diseases. BRD4 acetylates Lysine 122 on H3 (H3K122), a residue critical for nucleosome stability, resulting in nucleosome eviction and chromatin decompaction (Devaiah 2016). The intrinsically disordered regions (IDRs) of BRD4 are thought to facilitate its phase separation with coactivators such as MED1. The phase separation properties of BRD4 have been well-studied in several cell lines (Han 2020), and in the context of super-enhancers (Sabari 2018).

Need to add more information that we have found about BRD4 from current slide deck

Selective bromodomain inhibitors, such as JQ1 are often employed to displace BRD4 protein from chromatin (Filippakopoulos 2010). 1,6-hexanediol (1,6-HD), an aliphatic alcohol, can inhibit weak hydrophobic protein-protein interactions required for the droplet formation (droplet melting activity) and is widely used to elucidate the formation process of nuclear bodies (Duster 2021). However, the effects of BRD4, and phase separation at large, on the spatial structure of nucleosome nanodomains remains unclear. We envision a complementary approach, consisting of specific and non-specific inhibition of BRD4-containing condensates using small molecule drugs, to study the role of BRD4 in chromatin organization. Previous approaches to studying the dynamics of chromatin nanodomains only provide ensemble snapshots of chromatin structure, possibly due to slow acquisition times (Nozaki 2017).



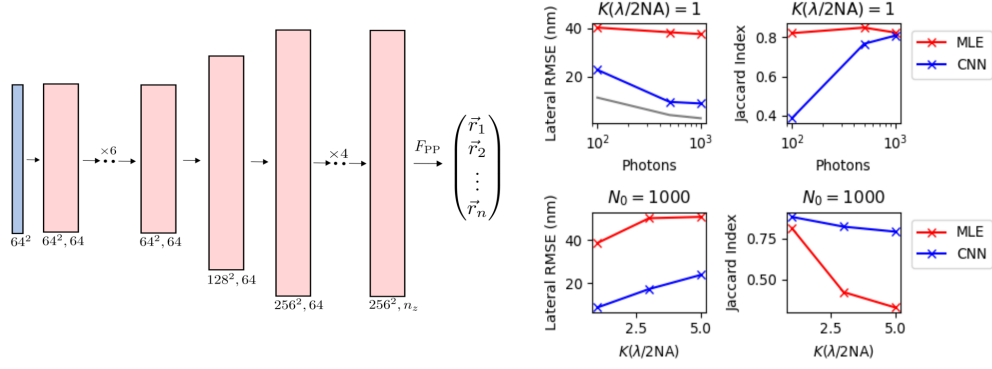


**Figure 3: Dense localization with deep learning** (A) Lateral and axial point spread functions of a single quantum dot at high ( $\sim 1.25$ ) and low ( $\sim 0.8$ ) numerical aperture (NA). (B) DeepSTORM3D convolutional neural network architecture used for localization. A monochrome image is convolved and upsampled to generate a localization map, which is post-processed to produce a vector of coordinates. (C) Lateral root mean squared error of maximum likelihood estimator (MLE) and a convolutional neural network (CNN) with respect to the incident photon count and the number of molecules within the diffraction limit  $\lambda/2NA$  for high NA. The Cramer-Rao lower bound on lateral uncertainty is shown in gray. Error samples =  $10^3$

## 0.2 Results

### 0.2.1 Novel approaches to time-resolved SMLM

Two major factors contribute to localization errors in SMLM: (i) the noise characteristics of CMOS cameras and (ii) crowding of molecules within a diffraction limited region. Maximum likelihood estimation (MLE) is frequently used for isolated molecules and high signal levels, retaining localization errors from 30-40nm (Figure 3c). However, MLE performance tends to degrade in low SNR and dense regimes where the number of emitters within the diffraction limit is greater than one ( $K(\lambda/2NA) > 1$ ). We employ a convolutional neural network DeepSTORM3D, which successively upsamples a monochrome image and outputs a localization map, which can be post-processed to produce molecular coordinates (Figure 2b). We demonstrate that this architecture can outperform maximum likelihood estimation for all signal levels and molecular densities tested (Figure 2c).

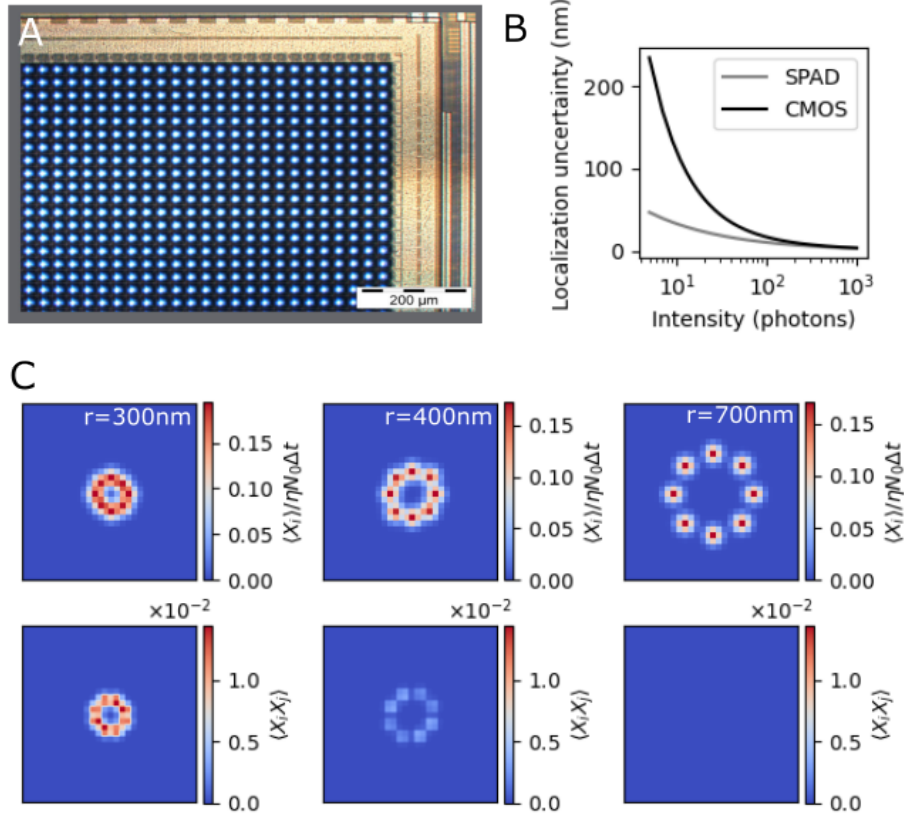


**Figure 4: Dense localization with fluorescence antibunching** (A) Lateral and axial point spread functions of a single quantum dot at high ( $\sim 1.25$ ) and low ( $\sim 0.8$ ) numerical aperture (NA). (B) DeepSTORM3D convolutional neural network architecture used for localization. A monochrome image is convolved and upsampled to generate a localization map, which is post-processed to produce a vector of coordinates. (C) Lateral root mean squared error of maximum likelihood estimator (MLE) and a convolutional neural network (CNN) with respect to the incident photon count and the number of molecules within the diffraction limit  $\lambda/2\text{NA}$  for high NA. The Cramer-Rao lower bound on lateral uncertainty is shown in gray. Error samples =  $10^3$

To generalize our imaging setup to three-dimensions, we could use that the lateral point spread function has a weak dependence on the axial coordinate (Figure 3a). However, it has been shown that the error around the focus can be large, while negative and positive defocus cannot be distinguished given the symmetric dependence in  $z$  (Holtzer 2007). Instead, we choose to introduce astigmatism into the detection path using a weak cylindrical lens (Figure 4a). In effect, this breaks the axial symmetry of the PSF and gives an anisotropic Gaussian which is elongated perpendicular to the optical axis. Localization proceeds by measuring this anisotropy and inverting a model of its axial dependence. At high numerical aperture, a strong dependence of the anisotropy to axial displacement potentially provides more precise three-dimensional localization (Figure 4b). In general, the axial anisotropy can be complex, but is often well described by a polynomial function of the axial displacement (Smith 2010). Unfortunately, astigmatic imaging increases the width of the point spread function significantly, exacerbating localization errors by molecular crowding and low signal to noise ratio. Therefore, we report error statistics for maximum likelihood based methods only, and leave three-dimensional localization with CNNs to future work. As one might expect, at ideal SNR, we show that axial dependence of localization error bears a strong similarity to the axial dependence of the PSF width (Figure 4c). Lateral RMSE can be maintained below 40nm for the anisotropic PSF for  $K(\lambda/2NA) \leq 5$ ; however, the Jaccard index tends to rapidly degrade at higher molecular densities, making MLE an unsuitable estimator for dense three-dimensional imaging (Figure 5). Three-dimensional single molecule tracking with sparse emitters remains a good application of this method, and will be used in future work.

### *0.2.2 Visualizing nucleosome clusters at super-resolution*

Here, we use the HaloTag system, a modified haloalkane dehalogenase designed to covalently bind to synthetic ligands (Los 2008). The HaloTag protein is fused to H2B, either through

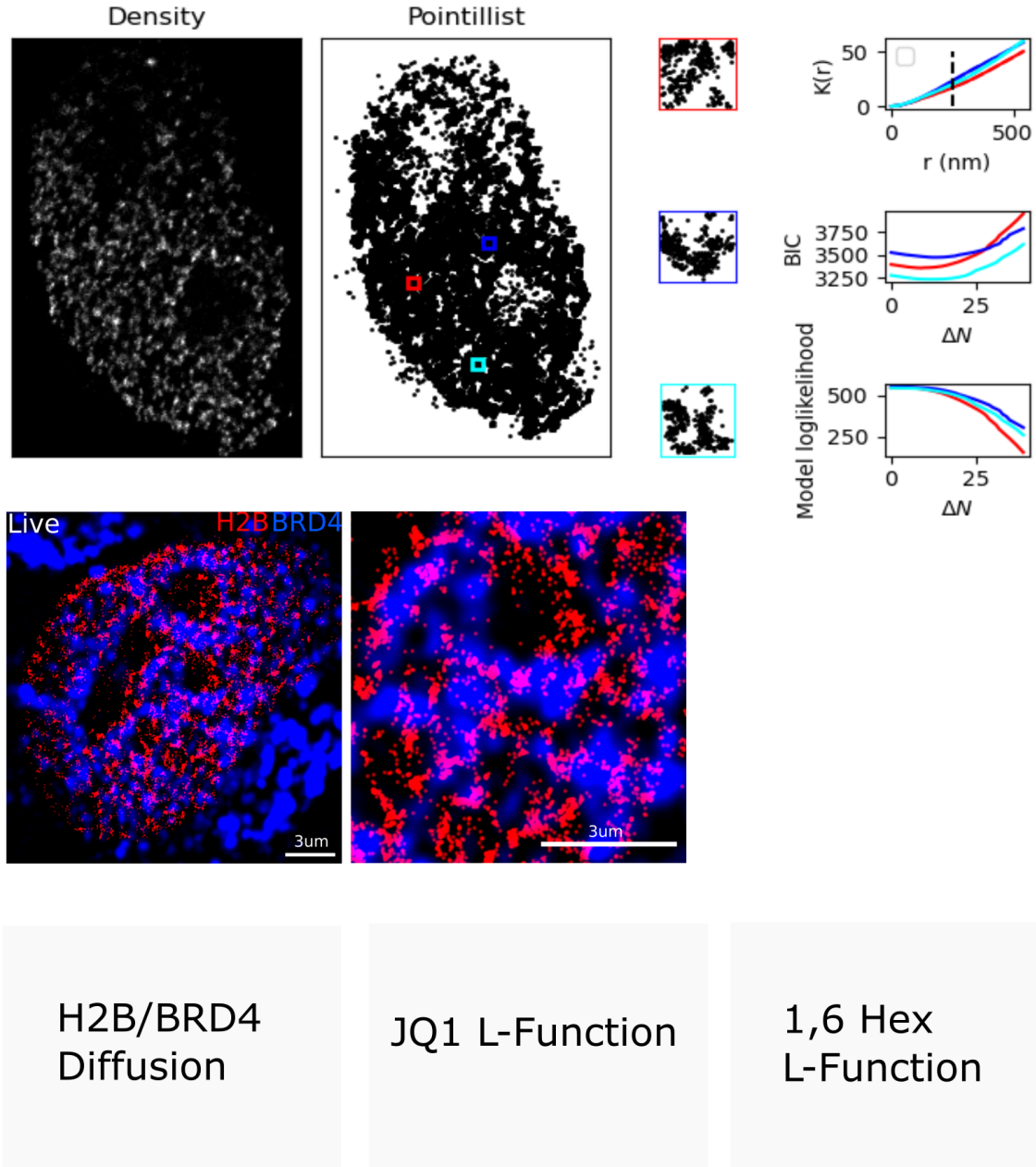


**Figure 5: Super-resolution reconstruction of nucleosome organization in a living HeLa cell nucleus.** (A) Density representation of nucleosome organization using 30nm x 30nm bins and a pointillist representation of nucleosome organization (B) Ripley's K function, Bayesian information criterion (BIC), and log likelihood for a Gaussian mixture model of pointillist localization data of three randomly selected regions of interest. Dashed line drawn at the diffraction limit (C) Localization accumulation over five seconds of imaging time (500 frames) and clustering with DBSCAN for a randomly selected region of interest

transfection and clonal selection, or by transient transfection. The HaloTag is bound by a rhodamine-derived fluorescent ligands, JF549 or JF646, in order to (Grimm 2015). For super-resolution or three-dimensional single molecule tracking, we use oblique illumination microscopy to illuminate a thin area within a single nucleus (Tokunga 2008; Nozaki 2017).

### 0.3 Future Aims

#### *0.3.1 Specific Aim 1: Measure nucleosome cluster dynamics in living cells*

##### Rationale and hypothesis

So far, super-resolved nucleosome clustering has been predominantly studied in fixed cells (Nozaki 2017; Itoh 2021). Live cell studies are limited by the low time resolution of SMLM and have so far relied on reconstruction of nucleosome reorganization by transforming wide-field images with convolutional neural networks. Using this technique, it has been reported that nucleosome clusters reorganize on millisecond to second time scales (Barth 2020). Therefore, we seek to apply our method to validate this result with fast two-color dSTORM microscopy on second time scales.

##### Experimental Approach

To perform this experiment, we have previously optimized simultaneous two-color labeling of H2B-HaloTag with JF549 and JF646. We maintain sparse labeling of H2B with JF549 using 10pM concentration and a short incubation time of 1 hour. The purpose of using JF549 is two fold: (i) Three-dimensional single molecule tracking can be performed on sparsely labeled samples with lower laser power than used in dSTORM (ii) Low laser power allows us to use this channel for autofocusing of the sample and performing cyclical imaging of the same living cell, with reduced photodamage. Moreover, we maintain dense labeling of

H2B-HaloTag with JF646 for super-resolution imaging of nucleosome clusters. Experiments will be carried out on a live cell microscope based on an Olympus IX83.

*0.3.2 Specific Aim 2: Determine effects of JQ1 and 1,6 Hexanediol exposure on nucleosome organization*

Rationale and hypothesis

Our previous results have validated the efficacy of JQ1 in inhibiting the expression of BRD4-controlled gene GBP5. This result is consistent with previous colocalization studies of the GBP locus with MED1 and BRD4 and identification of the GBP super enhancer (Lin 2022). JQ1 is a cell permeable small molecule that binds competitively to the acetyl-lysine binding cavity of BRD4, displacing BRD4 from chromatin (Fillappakopoulos 2010). BRD4 is known to play a role in nucleosome eviction as well as phase separation in nuclear bodies; however, it remains unclear the primary effects of BRD4 on nucleosome organization. JQ1 does indeed inhibit an array of genes, including GBP5 (Hogg 2017), but has had only a small effect on overall BRD4 residency in C33A nuclei (Han 2020). Therefore, it appears that the epigenetic role of BRD4 is more nuanced. For example, super-enhancers are far more sensitive to drugs blocking the binding of BRD4 to acetylated chromatin (Chapuy 2013; Loven 2013; Hnisz 2017). We hypothesize that large BRD4 aggregates are more susceptible to JQ1, while small aggregates can be dissolved with phase separation inhibitors, but not BET inhibitors alone.

1,6 Hexanediol exposure can rapidly induce broad reorganization of chromatin, providing a useful control for directly observing nucleosome cluster dynamics in mammalian cells. Nevertheless, changes in chromatin architecture following non-specific drugs can be difficult to decouple from induced changes in chromatin structure itself. Previous studies have demonstrated in fixed cells that nucleosome clusters are rapidly immobilized and condensed after exposure to 1,6 Hexanediol (Itoh 2021). However, nucleosome organization is highly

irregular, heterogeneous, and dynamic, making ensemble statistics inappropriate for making strong conclusions in fast perturbation experiments.

## Experimental Approach

JQ1 is a relatively slow acting small molecule drug. Therefore, we propose fixed cell experiments to validate its effect on BRD4 residency in the nucleus 2h, 4h, and 8h after exposure to 20uM JQ1. In fixed cell ensembles, we will measure size distributions of BRD4 clusters in control versus JQ1 treated cells. Later, we will transiently transfect BRD4-GFP fusion protein into HeLa cells followed by three-color live cell imaging of BRD4, H2B-JF549, and H2B-JF646 following initial exposure to 1-5 percent 1,6 Hexanediol. Cells will be exposed to Hexanediol on the microscope stage, followed by cyclic super-resolution imaging. This phase will be used to determine the effects of Hexanediol exposure on BRD4 residency in the nucleus and differential effects of Hexanediol on BRD4-positive and BRD4-negative chromatin nanodomains.

## 0.4 Materials and Methods

### *0.4.1 Super-resolution imaging of nucleosome nanodomains*

After transient transfection, H2B-HaloTag HeLa cells were incubated with JF646 HaloTag ligand overnight. Living HeLa cells were imaged in a dSTORM photoswitching buffer containing 100mM MEA, 50 ug/ml Glucose Oxidase, and 3.4 mg/ml Catalase (Sigma). Buffer pH was adjusted to 8 using HCl. Movies were collected using a custom Olympus IX83 microscope body equipped with an Olympus 60X 1.25NA oil-immersion objective. Images were projected onto an ORCA-Fusion sCMOS camera (Hamamatsu). The microscope was controlled using Micromanager software. JF646 molecules were illuminated with a 640nm laser held at 20mW, as measured at the back focal plane of the objective. Frames were captured

at 100fps. Registration of movies was performed with StackReg rigid body registration.

#### 0.4.2 Localization with maximum likelihood estimation

For each pixel, the number of photoelectrons  $S_k$  is multiplied by a gain factor  $g_k$  [ADU/ $e^-$ ], which generally must be measured during calibration. The readout noise per pixel  $\xi_k$  is Gaussian with some pixel-specific offset  $o_k$  (Figure 2a) and variance  $\sigma_k^2$  (Figure 2b). Ultimately, we have a Poisson component of the noise, which scales with the signal level and a Gaussian component, which does not. Therefore, in a single exposure, we measure:

$$\vec{H} = \vec{S} + \vec{\xi} \quad (1)$$

What we are after is the joint distribution  $P(\vec{H})$ . Fundamental probability theory states that the distribution of  $H_k$  is the convolution of the distributions of  $S_k$  and  $\xi_k$ ,

$$P(H_k|\theta) = P(S_k) \otimes P(\xi_k) \quad (2)$$

$$= A \sum_{q=0}^{\infty} \frac{1}{q!} e^{-\mu_k} \mu_k^q \frac{1}{\sqrt{2\pi}\sigma_k} e^{-\frac{(H_k - g_k q - o_k)^2}{2\sigma_k^2}} \quad (3)$$

where  $P(\xi_k) = \mathcal{N}(o_k, \sigma_k^2)$  and  $P(S_k) = \text{Poisson}(g_k \mu_k)$ ,  $A$  is some normalization constant and  $\otimes$  represents convolution. In practice, this expression is difficult to work with, so we look for an approximation. We will use the Poisson-Normal approximation to simplify Eq (4)

$$\xi_k - o_k + \sigma_k^2 \sim \mathcal{N}(\sigma_k^2, \sigma_k^2) \approx \text{Poisson}(\sigma_k^2)$$

Since  $H_k = S_k + \xi_k$ , we transform  $H'_k = H_k - o_k + \sigma_k^2$ , which is distributed according to



$$H'_k \sim \text{Poisson}(\mu'_k)$$

where  $\mu'_k = g_k \mu_k + \sigma_k^2$ . This result can be seen from the fact the the convolution of two Poisson distributions is also Poisson. The quality of this approximation will degrade with decreasing signal level, since the Poisson distribution does not retain its Gaussian shape at low expected counts. Nevertheless, the quality of the approximation appears to increase exponentially with the expected count, as measured by the Komogonov distance between the convolution distribution (4) and its Poisson approximation (Figure 2c).

Localization microscopy supposes that molecules really do have an exact location in space. In pratice, this is only an approximation since molecules can diffuse at physiological temperatures, and our exposure time would need to tend to zero for this to be exactly true. If we suppose that we can collect a sufficient amount of photons in a short enough time, such that a definite position exists, the following optimization problem is defined

$$\theta_{\text{MLE}} = \underset{\theta}{\operatorname{argmax}} \prod_k P(H_k|\theta) = \underset{\theta}{\operatorname{argmin}} - \sum_k \log P(H_k|\theta)$$

where  $\theta_{\text{MLE}}$  represents the maximum likelihood coordinates of a fluorescent molecule. Maximum likelihood estimation (MLE) is a natural choice, since optimization of coordinates under a Poisson likelihood is tractable. Under the Poisson approximation, the model negative log-likelihood is

$$\ell(\vec{H}|\theta) = -\log \prod_k \frac{e^{-(\mu'_k)} (\mu'_k)^{n_k}}{n_k!} \quad (4)$$

$$= \sum_k \log n_k! + \mu'_k - n_k \log (\mu'_k) \quad (5)$$

First order derivatives of the above sum can often be computed analytically, depending

on the spatial function  $\mu$ . The Poisson approximation is also convenient for computing the Fisher information matrix for  $\theta_{\text{MLE}}$  and thus the Cramer-Rao lower bound, which bounds the variance of a statistical estimator of  $\theta_{\text{MLE}}$ , from below (Chao 2016). Fisher information (separable case):

$$I_{ij}(\theta) = \mathbb{E} \left( \frac{\partial \ell}{\partial \theta_i} \frac{\partial \ell}{\partial \theta_j} \right) \quad (6)$$

Let  $\mu'_k = \mu_k + \sigma_k^2$ . For an arbitrary parameter,

$$\begin{aligned} \frac{\partial \ell}{\partial \theta_i} &= \frac{\partial}{\partial \theta_i} \sum_k x_k \log x_k + \mu'_k - x_k \log (\mu'_k) \\ &= \sum_k \frac{\partial \mu'_k}{\partial \theta_i} \left( \frac{\mu'_k - x_k}{\mu'_k} \right) \end{aligned}$$

$$I_{ij}(\theta) = \mathbb{E} \left( \sum_k \frac{\partial \mu'_k}{\partial \theta_i} \frac{\partial \mu'_k}{\partial \theta_j} \left( \frac{\mu'_k - x_k}{\mu'_k} \right)^2 \right) = \sum_k \frac{1}{\mu'_k} \frac{\partial \mu'_k}{\partial \theta_i} \frac{\partial \mu'_k}{\partial \theta_j}$$

### 0.4.3 Dense localization with convolutional neural networks

We employ a localization CNN architecture based on DeepSTORM3D which consists of three main modules. The first module consists of successive dilated convolutions, followed by an upsampling module to increase the lateral resolution by a factor of 4. The third and last module adds additional convolutional blocks to refine localization estimates. This architecture can also be used for three-dimensional localization and thus the final output has  $n_z$  channels. The final output is followed by an element-wise HardTanh (Maas 2013). A post-processing function  $F_{PP}$  uses a user-defined threshold to produce a matrix of coordinates. We find the performance of this architecture on simulated images surpasses MLE, and approaches the Cramer-Rao lower bound at high signal levels, retaining a RMSE near 20nm for  $K(\lambda/2\text{NA}) \leq 5$ , at high signal levels (Figure 3c).

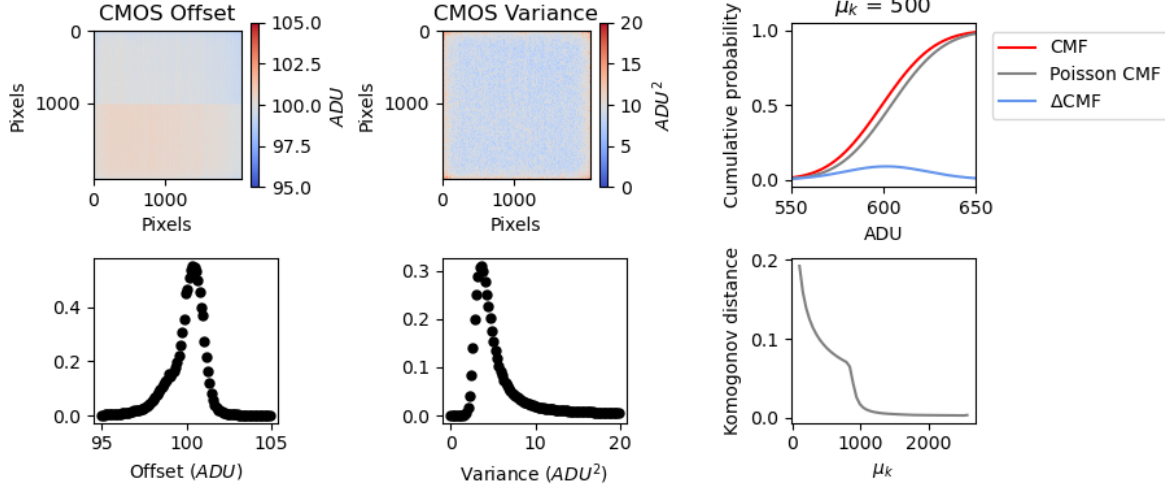


**Figure 6: Noise characterization of Hamamatsu ORCA-Flash 4 CMOS sensor.** (A) Offset for zero incident photons (B) Variance for zero incident photons (C) Cumulative mass function for the convolution distribution and its Poisson approximation for rate parameter  $\mu_k = 500$  counts (D) Komogonov distance measured as a function of rate parameter  $\mu_k$

#### 0.4.4 Dense localization by fluorescence antibunching

#### 0.4.5 Computation of Ripley's $L$ -function

#### 0.4.6 Fourier Ring Correlation

Following (Nieuwenhuizen 2013), a pair of subsets is drawn from the full list of localizations, and isotropic Gaussian kernel density estimation is performed. The Fourier Ring Correlation is calculated as a function of the ring radius  $q$  for two images  $f_1$  and  $f_2$

$$\text{FRC}(q) = \frac{\sum_{\vec{q} \in \text{circle}} \tilde{f}_1(\vec{q}) \tilde{f}_2(\vec{q})^*}{\sqrt{\sum_{\vec{q} \in \text{circle}} |f_1(\vec{q})|^2} \sqrt{\sum_{\vec{q} \in \text{circle}} |f_2(\vec{q})|^2}}$$

where  $\tilde{f}_1$  is the discrete Fourier transform of  $f_1$ .

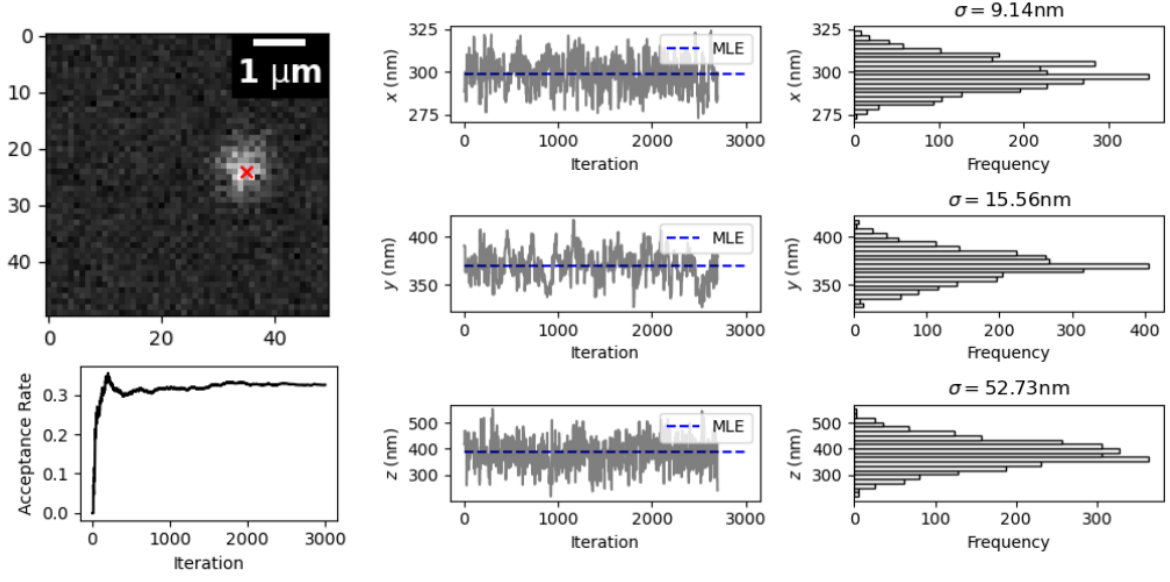


**Figure 7: Computing epistemic uncertainties with Metropolis-Hastings.** (top left) Simulated point spread function for  $N_0 = 10^3$  photons with a red x at  $x_{\text{MLE}}$  and  $y_{\text{MLE}}$  (bottom left) Acceptance rate of Markov chain (middle) Markov chains sampling from the posterior distribution on molecule coordinates in 3D, with the maximum likelihood estimation in dashed blue (right) Estimated posterior marginals on the localization parameters with their respective uncertainties

## 0.5 Supplemental Information

### 0.5.1 *Estimator precision sets the resolution limit in localization*

#### *microscopy*

Complementary Metal-Oxide-Semiconductor (CMOS) cameras have become a central tool in fluorescence microscopy. The CMOS sensor is revered for its high frame rates, allowing researchers to reach higher temporal resolutions. Nevertheless, CMOS cameras have noise sources intrinsic to their operation, such as shot noise and readout noise. The former phenomenon can describe a superposition of processes; namely, the fluctuations of the number of photons due to the quantum nature of light, and the random conversion of photons into photoelectrons within the semiconductor material with a quantum efficiency below unity. Here we will often refer to the photon count  $N_0$ , which has a determined value, rather than being described by statistically. The *measured* photon count, however, is well-described by a Poisson process (Schottky 1918). A shot-noise limited image with  $N$  pixels is then described as a family of Poisson variables, with units of photoelectrons

$$\vec{S} = [\text{Poisson}(\mu_1), \text{Poisson}(\mu_2), \dots, \text{Poisson}(\mu_N)] \quad (7)$$

CMOS sensors also suffer from other noise sources, such as readout noise or dark current, resulting in a nonzero signal even in the absence of incident light. Dark current is due to statistical fluctuations in the photoelectron count within a semiconductor material in thermal equilibrium. Fortunately, these additional noise sources are governed by the central limit theorem, and can be efficiently summarized as the component of the noise which exhibits a Gaussian distribution. Readout noise has been often neglected in localization algorithms because its presence in EMCCD cameras is small enough that it can be ignored within the tolerances of the localization precision. In the case of high speed CMOS cameras, however, the readout noise of each pixel is significantly higher and, in addition, every pixel

has its own noise and gain characteristic sometimes with dramatic pixel-to-pixel variations (Huang 2013). Therefore, accurate localization and simulation necessitates models which incorporate detailed sensor properties.

### 0.5.2 Integrated isotropic and anisotropic Gaussian point spread functions

For the sake of simplicity, it is common to describe the point spread function (PSF) as a two-dimensional isotropic Gaussian (Zhang 2007). This is an approximation to the more rigorous models given by Richards and Wolf (1959) or Gibson and Lanni (1989).

$$G(x, y) = \frac{1}{2\pi\sigma^2} e^{-\frac{(x-x_0)^2 + (y-y_0)^2}{2\sigma^2}}$$

The characteristic width  $\sigma$  of the PSF typically depends on the numerical aperture of the objective lens and The image of a fluorescent molecule captured by the objective lens, can be thought of as two-dimensional histogram of photon arrivals and a discretized form of the classical intensity profile  $G(x, y)$ . The value at a pixel approaches an integral of this density over the pixel:

$$\mu_k = i_0 \lambda_k = i_0 \int_{\text{pixel}} G(x, y) dx dy \quad (8)$$

Let  $(x_k, y_k)$  be the center of pixel  $k$ . If a fluorescent molecule is located at  $(x_0, y_0)$ , the probability of a photon arriving at pixel  $k$  per unit time reads

$$\lambda_k = \int_{x_k - \frac{1}{2}}^{x_k + \frac{1}{2}} G(x - x_0) dx \int_{y_k - \frac{1}{2}}^{y_k + \frac{1}{2}} G(y - y_0) dy$$

where  $i_0 = g_k \eta N_0 \Delta$ . The parameter  $\eta$  is the quantum efficiency and  $\Delta$  is the exposure time.  $N_0$  represents the number of photons emitted per unit time. We can then express the Gaussian integrals over a pixel by making use of the error function, giving a convenient

expression for the fraction of photons which arrive at a pixel  $k$

## 0.6 References

- [1] Schermelleh, L. et al. Super-resolution microscopy demystified. *Nature Cell Biology* vol. 21 72–84 (2019).
- [2] Speiser, A. et al. Deep learning enables fast and dense single-molecule localization with high accuracy. *Nat Methods* 18, 1082–1090 (2021).
- [3] Barth, R., Bystricky, K. Shaban, H. A. Coupling chromatin structure and dynamics by live super-resolution imaging. *Sci. Adv* vol. 6 (2020).
- [4] Chen, R. et al. Single-frame deep-learning super-resolution microscopy for intracellular dynamics imaging. *Nat Commun* 14, (2023).
- [5] Dertinger, T., Colyer, R., Iyer, G., Weiss, S. Enderlein, J. Fast, background-free, 3D super-resolution optical fluctuation imaging (SOFI). *PNAS*
- [6] Richards, B. Wolf, E. Electromagnetic Diffraction in Optical Systems. II. Structure of the Image Field in an Aplanatic System. Source: *Proceedings of the Royal Society of London. Series A, Mathematical and Physical Sciences* vol. 253 (1959).
- [7] Devaiah, B. N. et al. BRD4 is a histone acetyltransferase that evicts nucleosomes from chromatin. *Nat Struct Mol Biol* 23, 540–548 (2016).
- [8] Ouyang, W., Aristov, A., Lelek, M., Hao, X. Zimmer, C. Deep learning massively accelerates super-resolution localization microscopy. *Nat Biotechnol* 36, 460–468 (2018).
- [9] Filippakopoulos, P. et al. Selective inhibition of BET bromodomains. *Nature* 468, 1067–1073 (2010).
- [10] Chao, J., Sally Ward, E. Ober, R. J. Fisher information theory for parameter estimation in single molecule microscopy: tutorial. *Journal of the Optical Society of America A* 33, B36 (2016).
- [10] Grimm, J. B. et al. A General Method to Improve Fluorophores Using Deuterated

- Auxochromes. *JACS Au* 1, 690–696 (2021).
- [12] Nehme, E. et al. DeepSTORM3D: dense 3D localization microscopy and PSF design by deep learning. *Nat Methods* 17, 734–740 (2020).
- [13] Itoh, Y. et al. 1,6-hexanediol rapidly immobilizes and condenses chromatin in living human cells. *Life Sci Alliance* 4, (2021).
- [14] Han, X. et al. Roles of the BRD4 short isoform in phase separation and active gene transcription. *Nat Struct Mol Biol* 27, 333–341 (2020).
- [15] Tokunaga, M., Imamoto, N. Sakata-Sogawa, K. Highly inclined thin illumination enables clear single-molecule imaging in cells. *Nat Methods* 5, (2007).
- [16] Kalisvaart, D. et al. Precision in iterative modulation enhanced single-molecule localization microscopy. *Biophys J* 121, 2279–2289 (2022).
- [17] Zhang, B., Zerubia, J. Olivo-Marin, J.-C. Gaussian approximations of fluorescence microscope point-spread function models. (2007).
- [18] Los, G. V. et al. HaloTag: A novel protein labeling technology for cell imaging and protein analysis. *ACS Chem Biol* 3, 373–382 (2008).
- [19] Bannister, A. J. Kouzarides, T. Regulation of chromatin by histone modifications. *Cell Research* vol. 21 381–395 (2011).
- [20] Singh, R., Ghosh, D. Adhikari, R. Fast Bayesian inference of the multivariate Ornstein-Uhlenbeck process. *Phys Rev E* 98, (2018).
- [21] Holtzer, L., Meckel, T. Schmidt, T. Nanometric three-dimensional tracking of individual quantum dots in cells. *Appl Phys Lett* 90, (2007).
- [22] Ricci, M. A., Manzo, C., García-Parajo, M. F., Lakadamyali, M. Cosma, M. P. Chromatin fibers are formed by heterogeneous groups of nucleosomes in vivo. *Cell* 160, 1145–1158 (2015).
- [23] Hogg, S. J. et al. BET-Bromodomain Inhibitors Engage the Host Immune System and Regulate Expression of the Immune Checkpoint Ligand PD-L1. *Cell Rep* 18, 2162–2174



(2017).

- [24] Smith, C. S., Joseph, N., Rieger, B. Lidke, K. A. Fast, single-molecule localization that achieves theoretically minimum uncertainty. *Nat Methods* 7, 373–375 (2010).
- [25] Sabari, B. R. et al. Coactivator condensation at super-enhancers links phase separation and gene control. *Science* (1979) 361, (2018).
- [26] Linde, S. Van De et al. Direct stochastic optical reconstruction microscopy with standard fluorescent probes. *Nat Protoc* 6, 991–1009 (2011).
- [27] Huang, F. et al. Video-rate nanoscopy using sCMOS camera-specific single-molecule localization algorithms. *Nat Methods* 10, 653–658 (2013).
- [28] Ashwin, S. S., Nozaki, T., Maeshima, K. Sasai, M. Organization of fast and slow chromatin revealed by single-nucleosome dynamics. *Proc Natl Acad Sci U S A* 116, 19939–19944 (2019).
- [29] Hnisz, D., Shrinivas, K., Young, R. A., Chakraborty, A. K. Sharp, P. A. A Phase Separation Model for Transcriptional Control. *Cell* vol. 169 13–23 (2017).
- [30] Grimm, J. B. et al. A general method to improve fluorophores for live-cell and single-molecule microscopy. *Nat Methods* 12, 244–250 (2015).
- [31] Nozaki, T. et al. Dynamic Organization of Chromatin Domains Revealed by Super-Resolution Live-Cell Imaging. *Mol Cell* 67, 282-293.e7 (2017).
- [32] Xu, J. et al. Super-Resolution Imaging of Higher-Order Chromatin Structures at Different Epigenomic States in Single Mammalian Cells. *Cell Rep* 24, 873–882 (2018).
- [33] Boettiger, A. N. et al. Super-resolution imaging reveals distinct chromatin folding for different epigenetic states. *Nature* 529, 418–422 (2016).
- [34] Nozaki, T. et al. Dynamic Organization of Chromatin Domains Revealed by Super-Resolution Live-Cell Imaging. *Mol Cell* 67, 282-293.e7 (2017).
- [35] Nieuwenhuizen, R et al. Measuring image resolution in optical nanoscopy. *Nature Methods* 10. 557-562 (2013).